

Ultrasonic displacement measurements from local absorption of ultrasound in thermochromic liquid crystal sensors

M. Turvey^{a,*}, O. Trushkevych^b, D.J. McKnight^c, R.S. Edwards^a

^a Department of Physics, University of Warwick, CV4 7AL, UK

^b School of Engineering, University of Warwick, CV4 7AL, UK

^c Pictura Bio, Wood Centre for Innovation, Quarry Road, Oxford, OX3 8SB, UK

ARTICLE INFO

Keywords:

Liquid crystal
Ultrasound sensor
Wavefield imaging

ABSTRACT

Wavefield imaging can be used for measuring the wavefield produced by an ultrasound transducer for medical and industrial applications, or for the detection and monitoring of defects in non-destructive testing. Typical wavefield imaging methods include interferometry/vibrometry, and the use of microphones and hydrophones. These involve scanning, making them time consuming, and microphones have limited resolution. An alternative method presented here uses thermochromic liquid crystal sensors which react to heat generated due to absorption of ultrasonic waves. The result is a colour scale that varies with temperature, with the temperature change dependent on ultrasonic displacement. Measurements of the resonant modes of a flexural ultrasonic transducer were taken between 320 kHz and 6.77 MHz. Temperature maps were obtained from photographs of the TLC sensor using the true-colour image processing method. The obtained temperature change across the transducer face was compared with displacement measurements taken using interferometry, showing excellent agreement in the position of the mode features and good resolution at lower frequencies. Thermal measurements were also taken to directly observe the heating of the transducer cap, showing the effect of the thermal conductivity of the transducer along with confirming the increased heat generated by the ultrasound absorption when a backing layer is used. The sensors show promise for fast transducer characterisation, with further potential applications in structural health monitoring and defect detection.

1. Introduction

Wavefield imaging refers to the capture of waveform data over an area of interest, in order to produce an image [1]. 2D imaging of wavefields is of importance for applications such as transducer characterisation, which can include measuring the profile or mode of the wavefield produced by transducers in both medical and industrial fields [2–5]. This is important for safety reasons, by ensuring transducers are performing as expected. It can also be used for reliable testing of infrastructure for non-destructive testing (NDT) and structural health monitoring, by observing how the wavefield changes in the presence of defects. It contributes to the understanding of how waves interact with structural features and defects within different samples [1,6–8].

The gold standard method for wavefield imaging on the surface of solid samples is laser vibrometry or interferometry, which measure the velocity or displacement of the surface at a point. To build an image, the laser is scanned across the surface [8–11]. These methods have a high sensitivity and dynamic range, are broadband in their operation,

and can provide detailed information in addition to the displacement, such as the frequency of oscillations [11]. However, point-by-point scanning across the surface is required to build up an image, resulting in a time consuming process with resolution limited by step size and focal point size [11]. The methods also require the use of expensive and potentially not eye safe equipment, with additional costs for shear wave detection, making them less accessible for small-medium enterprises (SMEs).

The use of microphones and hydrophones are more moderate cost methods for imaging wavefields in air or water, however, they also require scanning which results in similar time constraints. They have a high frequency and dynamic range, however, they have no shear wave detection capability since most fluids are unable to support shear waves, and resolution is similarly limited by step and detector size [12, 13]. An alternative method which will work for optically transparent and anisotropic media is photoelasticity, which uses crossed polarisers

* Corresponding author.

E-mail addresses: m.turvey@warwick.ac.uk (M. Turvey), r.s.edwards@warwick.ac.uk (R.S. Edwards).

<https://doi.org/10.1016/j.ultras.2024.107352>

Received 12 February 2024; Received in revised form 26 April 2024; Accepted 18 May 2024

Available online 23 May 2024

0041-624X/© 2024 The Authors. Published by Elsevier B.V. This is an open access article under the CC BY license (<http://creativecommons.org/licenses/by/4.0/>).

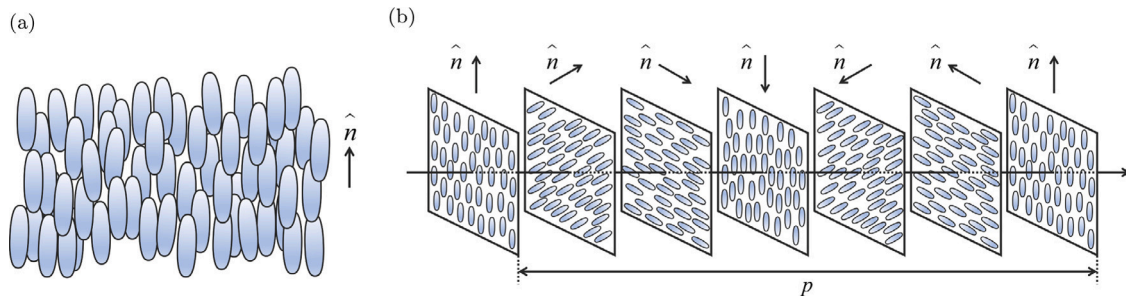


Fig. 1. (a) Nematic and (b) cholesteric liquid crystal structures. \hat{n} indicates the director axis of the liquid crystal molecules and p is the pitch of the cholesteric liquid crystal structure.

placed on either side of a sample, along with a stroboscope to allow for the capture of fast moving waves, to visualise birefringence caused by stress/strain in the sample [14,15]. This method removes the need for time consuming scans, however, the limitations make it unsuitable for the majority of NDT applications.

Acoustography [16–19] and paint-on/removable sensors based on polymer-dispersed liquid crystals (PDLCs) [20–22] or thermochromic liquid crystals (TLCs) [23–28] have been suggested as alternative wavefield visualisation techniques. These are all methods that make use of the unique optical properties of liquid crystals. A liquid crystal is an intermediate state of matter that exhibits the properties of both isotropic liquids and crystalline solids [29]; it has flow like a liquid, but anisotropy and order like a crystal. Liquid crystal materials contain rod-like molecules which have both orientational and positional ordering [29]. These molecules are generally aligned along the same axis, known as the director axis \hat{n} , with the positional ordering resulting in different structures of LC. The most common structure is nematic, where the molecules are randomly positioned (Fig. 1(a)) [29].

Acoustography uses a thick layer of aligned nematic LC as an area sensor to convert ultrasound into an image in real time, with no scanning required [16–19]. A sample is placed into a water bath between a plane wave transducer and the LC sensor. When exposed to ultrasound, the LC molecules in the sensor realign, which changes the optical properties of exposed area and is visible when viewed through polarisers. This technique is currently limited to operation at 3.3 MHz, and requires oblique incidence of the ultrasound upon the sensor, along with needing crossed polarisers for the effect to be visible.

Thin LC ultrasound sensors that remove the need for polarisers and water baths have been suggested [20–28]. PDLC sensors contain droplets of randomly aligned nematic LC dispersed in a polymer matrix, with the refractive index of the droplets when aligned chosen to match that of the polymer [29]. When no field is present, the PDLC scatters light and appears cloudy, however, upon application of a field the LC droplets align, allowing light to pass through the film and hence it appears transparent [21,22]. The dynamic range of the sensor is limited, particularly at frequencies below 1 MHz, and there is a sharp on–off switching characteristic which limits the displacement information that can be obtained, however results showed excellent promise for LC-based acoustic sensors which can be removed from water baths [22].

Alternatively, TLC based sensors can be used [23–28]. These use a structure of LC called cholesteric/chiral nematic, which consists of layers of nematic LC arranged with their director axis in a helical structure, shown in Fig. 1(b) [29]. The distance between layers with parallel director axes is the pitch, and for TLCs this varies with temperature [30]. When placed in an ultrasound field, there is absorption of the acoustic wave at the interface between the surface and sensor, leading to a change in temperature which depends on the ultrasonic displacement, among other factors such as frequency and coupling between sample and sensor [24,25,31]. Light selectively reflects off the helical structure when the wavelength matches the pitch, providing a colour scale that varies with temperature and therefore ultrasonic

displacement [29,30]. The use of a colour scale results in more detailed displacement information than acquired when using a PDLC sensor. Both PDLCs and TLCs can be used to make passive, broadband, low cost sensors that require no surface scanning [21,22,31]. They do not require the use of polarisers or a water bath, and are visual sensors so will be compatible with robotic vision, allowing for possible future automation. Research into the use of TLCs for ultrasound detection was predominantly conducted in the 1970s, in particular for transducer characterisation [23–26], however, this was mainly done in water baths and was largely qualitative. More recently, TLC films have been used to map the focal spot of a concave transducer [27], however quantification of the ultrasonic displacement from the film was not shown.

In this paper we show the use of compound TLC sensors, consisting of a LC layer and an absorbing backing layer, for comparative ultrasonic displacement measurements and wavefield visualisation. Quantitative temperature measurements are obtained from optical photographs of the sensor, which are then compared to displacement measurements obtained by interferometry. Thus a method to obtain quantitative measurement of displacement from an optical image of the sensor is developed. The thermal behaviour of the compound sensor is also studied through thermal camera measurements. This offers an understanding of the behaviour of the compound sensors, along with a method for in-situ characterisation of the obtained results.

2. Methodology

2.1. Experimental set-up

An initial compound sensor was built using a commercial TLC sheet [32] with a backing layer of thickness 0.25 ± 0.02 mm to aid in the absorption of ultrasound. The TLC sheet consisted of 3–5 μm liquid crystal droplets dispersed in a polymer matrix and sandwiched between two mylar sheets. It had a thickness of 0.163 ± 0.02 mm and an operating temperature range of 25–30 $^{\circ}\text{C}$, over which it changed from red to blue, with red starting at 25 $^{\circ}\text{C}$, green starting at 26 $^{\circ}\text{C}$, and blue starting at 30 $^{\circ}\text{C}$, as shown by the calibration curve shown in Fig. 2. Although there is some colour response in the 30–44 $^{\circ}\text{C}$ range, this is in a wavelength range at the edge of the visible light spectrum and is therefore difficult to measure. The sheet had a black background for contrast meaning the sensor appeared black when outside the operating temperature range. Other choices of TLC material are available that operate in different temperature ranges; this particular choice was made based on typical laboratory conditions and the expected temperature rise due to ultrasound absorption.

The backing layer side of the sensor was coupled using ultrasound gel to a flexural ultrasonic transducer, which oscillates in different resonant modes with the fundamental at 40 kHz [33]. The flexural transducer consisted of an aluminium cap of diameter $a = 25$ mm and thickness $h = 0.6$ mm, with a piezoelectric element of diameter 9 mm bonded to the back, sealed in an air cavity by a silicone backing layer [33]. A cross-sectional schematic of the sensor and transducer

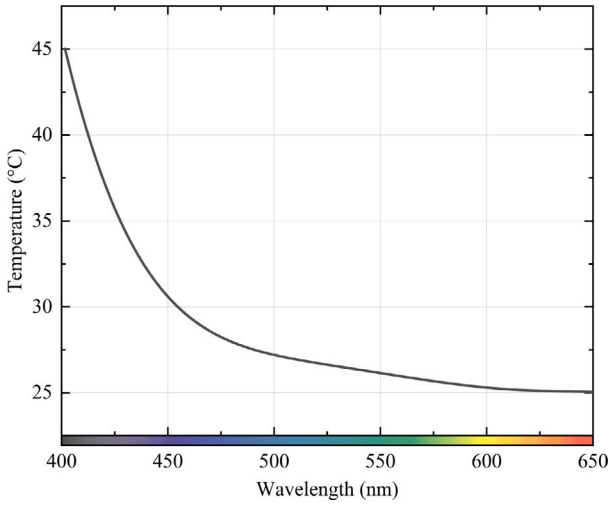


Fig. 2. Temperature against wavelength for the liquid crystal sheet used, with operation temperature 25–30 °C [32].

is given in Fig. 3. At certain frequencies the cap resonates, producing distinctive modal patterns with nodal rings and lines (positions of zero displacement), with increasingly complex modal patterns as frequency is increased.

The resonant frequencies can be approximated as those of a circular plate with clamped edges [33], with frequencies $f_{m,n}$ given by [34]

$$f_{m,n} = \frac{1}{2\pi} \left(\frac{\lambda_{m,n}}{a} \right)^2 \sqrt{\frac{D}{\rho}}, \quad (1)$$

where (m, n) is the mode indicated by the number of nodal circles, m , and nodal lines, n , $\lambda_{m,n}$ is a numerically calculated mode constant, a is the plate diameter, and ρ is the density. D is the flexural rigidity, the resistance given by the plate as it bends,

$$D = \frac{Eh^3}{12(1-\nu^2)}, \quad (2)$$

where E is young's modulus, h is the plate thickness, and ν is Poisson's ratio. Values of $\rho = 2710 \text{ kg m}^{-3}$, $\nu = 0.31$, and $E = 70 \text{ GPa}$ were used for the aluminium cap, with cap dimensions $a = 25 \text{ mm}$ and $h = 0.6 \text{ mm}$ [33]. The cap was excited at frequencies from $320 \pm 10 \text{ kHz}$ to $6.77 \pm 0.01 \text{ MHz}$ to show broadband operation over a typical range of frequencies for NDT, with this range containing a suitable number of resonant modes.

A schematic of the set-up used for TLC measurements is shown in Fig. 4(a). The flexural transducer was driven by a continuous sine wave, using a function generator and a 25 W radio frequency (RF) amplifier. A $\times 10$ attenuator was used on the signal from the function generator to protect the amplifier. The frequency was changed to find the resonant modes and the driving voltage was varied between 0.2 to 2.5 V peak-to-peak. This controlled the mode-dependent displacement, with the output power to the transducer varying between 3–5 W. At lower frequencies, larger driving voltages/higher power signals are required. This can be understood from Stokes' law of sound attenuation [35]

$$A(z) = A_0 \exp\left(-\frac{z}{2\lambda}\right), \quad (3)$$

where $A(z)$ is the amplitude at depth z , A_0 the amplitude at the surface, and λ is wavelength. For lower frequencies, less of the ultrasound is absorbed (attenuated) by the sensor, so more power is required for visualisation. For significant absorption of ultrasound, the absorber thickness should be at least $\lambda/10$ [36]. At 320 kHz the thickness is approximately $\lambda/11$, changing to $\lambda/2$ at 6.77 MHz, resulting in better absorption of ultrasound at higher frequencies.

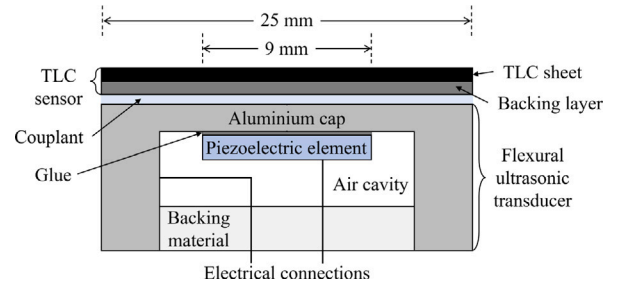


Fig. 3. Cross-sectional schematic of the flexural transducer and the TLC sensor.

Videos of the transducer heating up once a sufficient voltage (displacement) was reached were taken using a Canon R6 camera with a Canon EF 100 mm f/2.8 Macro lens. The imaging time for the modes was between 10 to 30 s, including time taken for the surface to warm into the temperature range of the sensor. The lower frequency modes took longer to visualise since less ultrasound is absorbed in the sensor (Eq. (3)). A tripod was used for stability and the lighting was kept even and consistent across the transducer face, with a colour temperature of 6500 K. Colour temperature gives a value for how warm (red) or cool (blue) lighting is, with 6500 K located in the white light region [37]. Frames from the video were extracted for further analysis, with the video also being used to explore more general thermal background effects arising from the thermal conductivity of the cap and sensor. Temperature was extracted from the images as described in Section 2.2. The sensor is completely reversible, with the mode pattern disappearing in seconds when ultrasound excitation stops.

Displacement measurements of the flexural transducer without the TLC sensor were taken using an Intelligent Optical Systems (IOS) two-wave mixer interferometer for comparison with the temperature data obtained from the TLC sensor. A schematic is shown in Fig. 4(b). Interferometry was chosen over vibrometry due to the increased sensitivity and need for absolute displacement measurements, which interferometry measures directly. An XY stage was used to scan the focal point of the interferometer over two perpendicular lines across the diameter of the transducer, as shown in Fig. 4(c). The displacements measured along the two lines were averaged to reduce any effects caused by the uneven bonding of the piezoelectric element to the cap.

Finally, a Cedex Titanium 20 thermal camera was used to explore the heating of the cap caused by mechanical motion and thermal conductivity at various resonant frequencies. The set-up was the same as that of the TLC measurements, shown in Fig. 4(a). Videos were first taken with a layer of black paint on the cap to provide constant emissivity over the surface, in order to image general heating of the cap during operation, and then taken again with the sensor's backing layer to observe the difference between the heat produced by mechanical motion of the transducer cap and the heat absorbed in the backing layer due to the ultrasonic field. The videos were taken inside an enclosure to remove the effects of thermal reflections from body heat. No thermal images were taken of the full compound sensor due to its reflective front face.

2.2. Temperature map extraction

The colour displayed on the TLC sensor due to reflected wavelength is related to temperature via the calibration curve shown in Fig. 2. Direct measurement of the wavelength reflected from the sensor is not possible without the use of specialised equipment such as a spectrophotometer [38], which is not generally available in situations where these sensors may be used. In addition, the colour perceived will vary depending on the light source used for viewing [37], so this must be taken into consideration. Instead, the true colour image processing method outlined in Fig. 5 was followed in order to convert RGB values

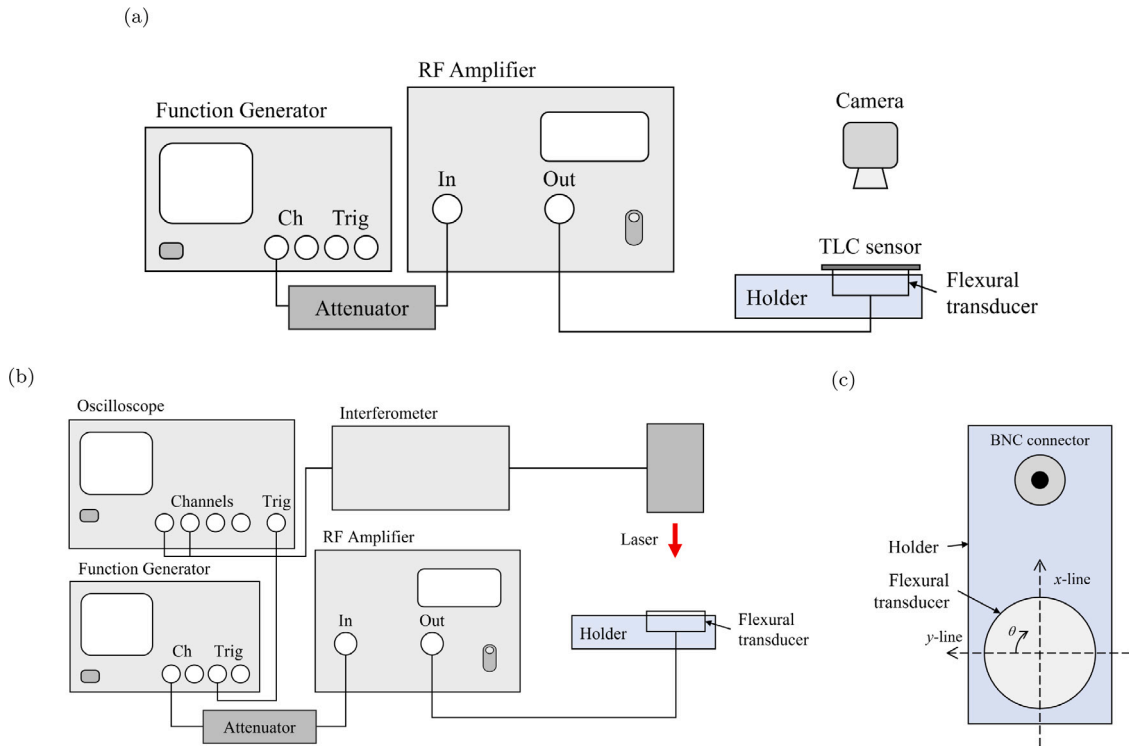


Fig. 4. Schematic of (a) the TLC and thermal camera experimental set-up, (a) the interferometer experimental set-up, and (c) a birds-eye view of the transducer and holder with the scan directions of the xy stage for the interferometer measurements.

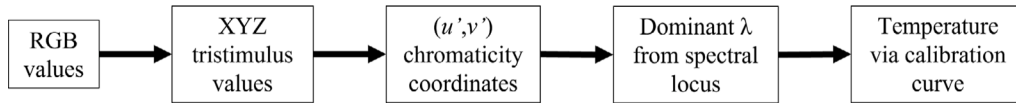


Fig. 5. Flowchart of the process for obtaining temperature data from photos of the TLC sensor.

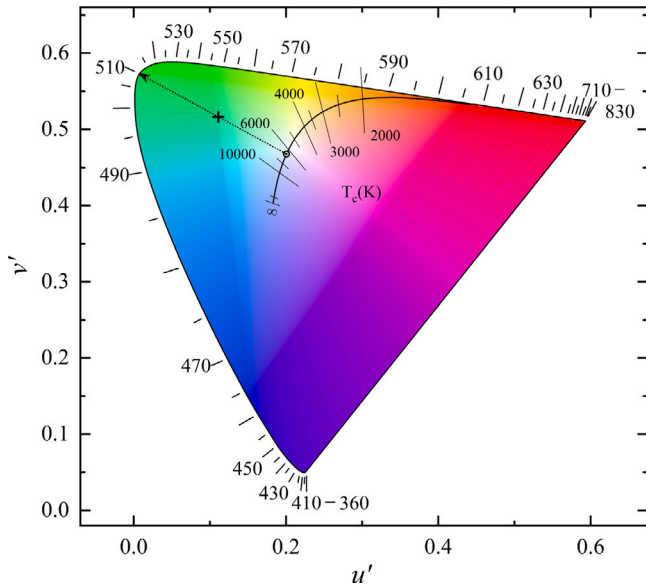


Fig. 6. The CIE 1976 colour space chromaticity diagram. The curved outer boundary (spectral locus) displays dominant wavelength chromaticity coordinates in nm. The inner dashed line (Planckian or black body locus) shows the chromaticity coordinates of the colour temperature of a black body in Kelvin, where the lines crossing the locus are correlated colour temperature (CCT).

taken from videos and photographs of the sensor into a measure of the dominant wavelength, using the CIE 1976 chromaticity diagram (Fig. 6).

For each pixel in the photos of the TLC sensor, the RGB value was converted to XYZ values using the MATLAB function 'rgb2xyz'. The CIE XYZ colour space is an imaginary colour space that is device-independent and therefore typically used for conversion between other colour spaces [37,39]. These XYZ values were then converted into chromaticity coordinates (u' , v') using

$$\begin{aligned} u' &= \frac{4X}{X + 15Y + 3Z} \\ v' &= \frac{9Y}{X + 15Y + 3Z} \end{aligned} \quad (4)$$

Chromaticity is a definition of a colour that uses hue and saturation, regardless of luminosity [40], meaning for example a light and dark red can have the same chromaticity coordinates despite having different luminosities arising from viewing light intensity. The CIE 1976 chromaticity diagram (Fig. 6) represents the chromaticities of different colour stimuli, defined by chromaticity coordinates (u' , v'). The outer curve is the spectral locus and gives the chromaticities of monochromatic colour stimuli at full saturation, along with their corresponding dominant wavelength which is related to hue. The inner curve is the Planckian or blackbody locus, and provides the chromaticities of light sources that approximate black-body radiators across the range of colour temperatures. The chromaticity coordinate of the light source used for viewing is referred to as the white point.

To determine wavelength, a straight line is drawn from the white point of the light source through the chromaticity coordinate of the

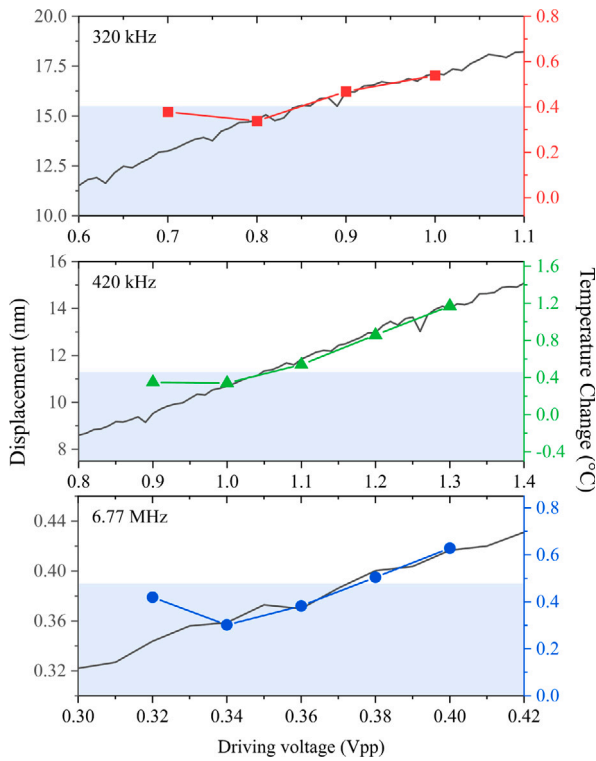


Fig. 7. Comparison of displacement measurements taken using interferometry (right axes) with temperature change across the TLC sensor (left axes), for increasing driving voltages at 320 ± 10 kHz, 420 ± 10 kHz, and 6.77 ± 0.01 MHz. The blue box shows the region where displacements were too small to be observed using the TLC sensor, giving the minimum sensitivity.

pixel and extended to the spectral locus. An example of this is shown on Fig. 6, with the whitepoint indicated by a dot on the blackbody locus and the pixel chromaticity by a +. The dominant wavelength for the pixel is determined from the point at which this line intersects the spectral locus [41]. This wavelength value was then converted to temperature using the calibration curve in Fig. 2.

Before the temperature analysis was performed, filtering was applied to the photos. The saturation value, which describes the intensity of the colour, was used to remove gray-scale pixels which are outside the range of the sensor. Intensity I and saturation S are given by

$$I = \frac{R + G + B}{3}$$

$$S = 1 - \frac{\min(R, G, B)}{I} \quad (5)$$

Saturation values less than 0.15 were filtered out, and then a moving averaging window of 5×5 pixels (px) for video frames of size 914×914 px was applied to reduce noise, where 1 px corresponds to 30 μm .

3. Results and discussion

3.1. TLC temperature maps

Fig. 8 shows images of the TLC sensor on the flexural transducer for several of the resonant modes, for frequencies ranging from 320 ± 10 kHz to 6.77 ± 0.01 MHz. Mode frequencies for lower frequency modes were confirmed using numerical modelling; at higher frequencies the modes overlap. The sensor reacts to heat generated by local absorption of ultrasound, and hence areas of higher temperature indicate antinodes, with the colourful rings and lines indicating both peaks and troughs in displacement for the mode pattern.

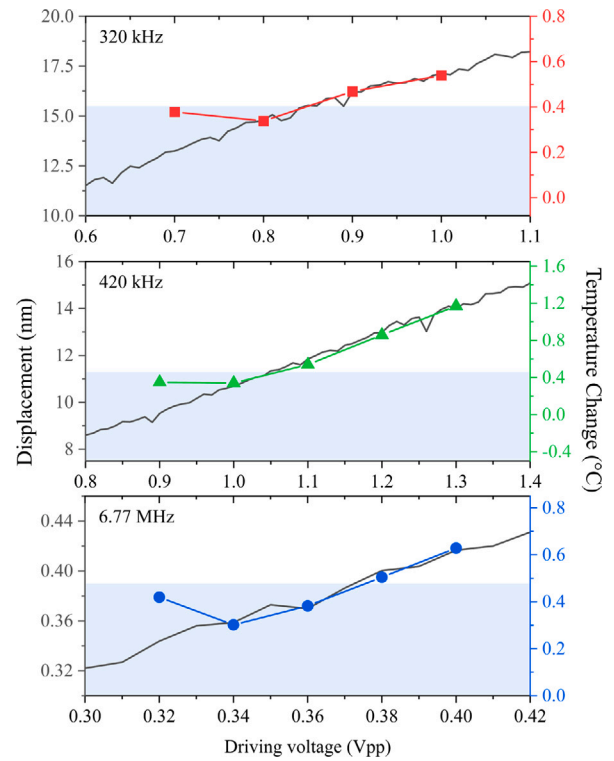


Fig. 8. Photographs of the flexural ultrasonic transducer resonant modes visualised using the TLC sensor at frequencies of (a) 320 ± 10 kHz, (b) 420 ± 10 kHz, (c) 740 ± 10 kHz, (d) 4.7 ± 0.01 MHz, and (e) 6.77 ± 0.01 MHz. The sensor operates from red at 25 °C through to blue at 30 °C.

The displacement at the centre of the transducer was measured using the interferometer as a function of driving voltage, for three different modes. The frequency given is that of the resonance measured using the TLC sensor; note that the resonant frequency of the transducer without the sensor is slightly higher. Photographs of the TLC sensor were taken for several driving voltages for each mode around the point where the sensor began to show sensitivity, with the temperature change at the centre extracted using image analysis. Fig. 7 shows the data obtained in these measurements. For these low driving voltages, the sensor is dark (near black), leading to some errors in the analysis. Detectability was therefore set at the point where a clear change was measured. The blue boxes show displacements which were too small to be observed. At 320 ± 10 kHz the sensitivity was found to be 15.5 ± 0.1 nm, increasing to 0.39 ± 0.02 nm at 6.77 ± 0.01 MHz, which follows previous work using PDLC sensors [22].

Nodal rings are visible in all the modes measured, and are clear across the whole cap for the modes at 320 ± 10 kHz and 420 ± 10 kHz (in Figs. 8(a) and 8(b), which show modes (0,6) and (0,7) respectively). At higher frequencies, different modes can occur at similar frequencies resulting in mode-mixing and therefore more complex patterns [33]. For the mode at 740 ± 10 kHz in Fig. 8(c) the mode shape displays nodal lines, indicated by the alternating lighter and darker sections around the circumference of the transducer. For the mode at 4.7 ± 0.01 MHz in Fig. 8(d), the modal pattern seen is due to the separate resonances of the piezoelectric element and the cap; the central rings cover the area where the element is glued, and have a larger amplitude than the outer rings that cover the rest of the cap. Finally, for the mode at 6.77 ± 0.01 MHz shown in Fig. 8(e), large amplitude rings can be seen over the area where the piezoelectric element is attached to the cap, with some rings seen outside this area, indicating that the cap is oscillating but the majority of the heat generated by the displacement is located at the centre of the transducer; this is possibly because at this

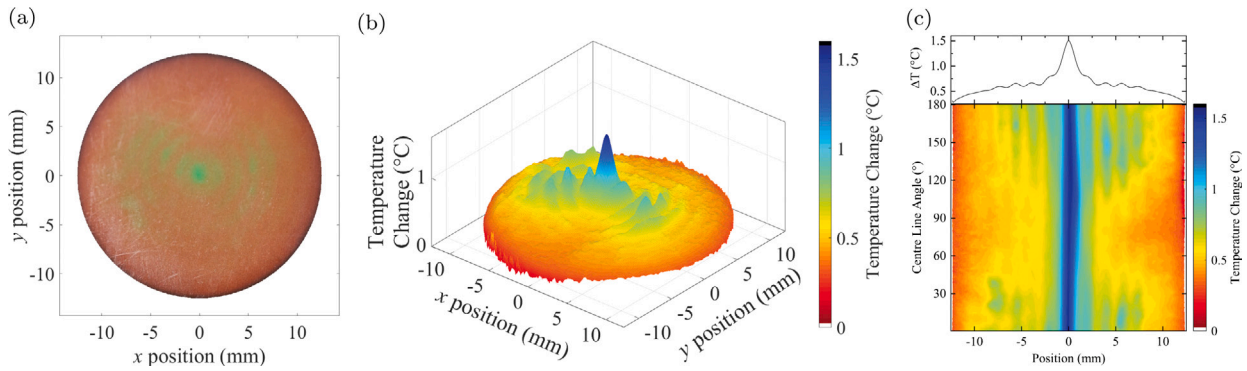


Fig. 9. The 320 ± 10 kHz resonant mode showing (a) analysed image, (b) 3D temperature map of transducer surface, and (c) the centre lines of the mode from position $y = 0$ in the clockwise direction.

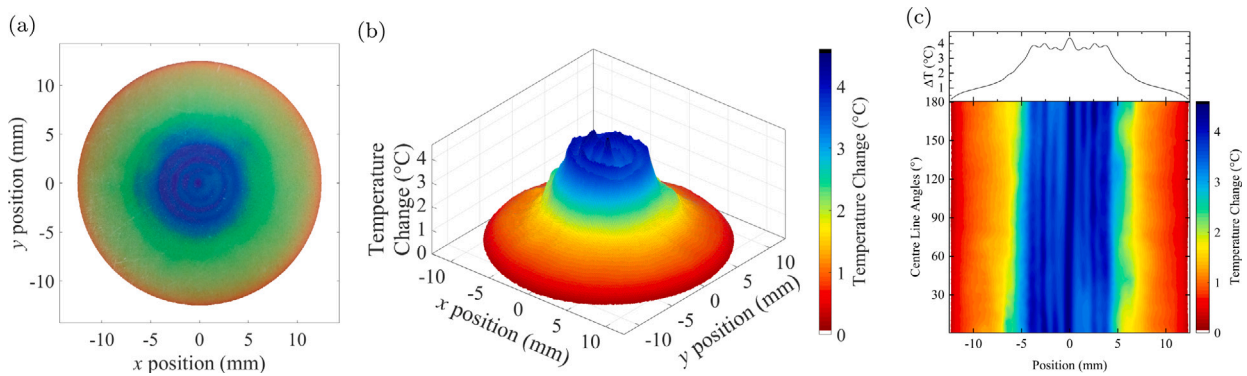


Fig. 10. The 6.77 ± 0.01 MHz resonant mode showing (a) analysed image, (b) 3D temperature map of transducer surface, and (c) the centre lines of the mode from position $y = 0$ in the clockwise direction.

frequency the piezoelectric element resonates with significantly greater amplitude than the cap. The outer rings would therefore be hidden due to thermal conductivity of the cap and the LC sensor, which leads to lateral diffusion of heat obscuring anti-nodal rings that are small in amplitude and less than 1 mm apart [28].

Temperature change is related to ultrasonic displacement, as well as factors such as the coupling and the frequency of operation. Therefore one cannot obtain the absolute temperature of the cap, however, the comparative displacement across the face of the transducer cap can be obtained by measuring the temperature change after absorption of the ultrasound. The images selected for analysis are shown in Figs. 9(a) and 10(a) for two modes at 320 ± 10 kHz and 6.77 ± 0.01 MHz. These frames were analysed using the method laid out in Section 2.2. Different video frames were chosen for this analysis than those displayed in Fig. 8; the eye has better contrast for a black background, but for analysis having few black pixels (regions outside the temperature sensitivity of the sensor) is beneficial. Pixels below a saturation of 0.15 (Eq. (5)) were removed from the photograph before analysis to remove any remaining black background. This would also remove anomalous values from any white marks, visible at the edge of the photos in Fig. 8, caused by the scattering of incident light by scratches on the top surface of the sensor. The largest error in temperature analysis should usually arise from any changes in lighting during the measurement process, however, since the set-up was stable this did not have any major effects on the calculated value. Instead approximate errors, calculated from the average difference between temperature change across each frame in the videos, have been used.

The extracted temperature map for the 320 ± 10 kHz resonance shown in Fig. 9(b) clearly shows the anti-nodal rings, along with the central area of greater displacement; note that colour of the map has been chosen to mimic the colour-range of the TLC sensor, with blue indicating hotter regions. The largest temperature change across the

transducer face was 1.53 ± 0.02 °C. To analyse the mode shape, the temperature change across the transducer face diameter was taken, with results shown in Fig. 9(c). The colour-map shows the temperature change for multiple diameters plotted as a function of the angle of the diameter line relative to the x -axis (defined in Fig. 4(c)). The unevenness of the modal pattern across the transducer face can be seen by the variation in the temperature change as the analysis line angle is changed. This is due to the unevenness of the bond between the piezoelectric element and the transducer cap, along with thickness variations in the cap and piezoelectric element. At the top of the figure, an average of the extracted diameter temperature profiles is given. The peaks of this average line correspond to the anti-nodal circles of the mode.

Similarly, for the mode at 6.77 ± 0.01 MHz the temperature map and the temperature profile across multiple diameters are shown in Figs. 10(b) and 10(c). For the temperature map, the inner anti-nodal rings are clearly visible with at least two fainter rings outside of this region, partially concealed by the lateral diffusion of heat in the sensor due to the thermal conductivity of both the cap and LC sensor. For this mode the largest temperature change is 4.48 ± 0.03 °C. The unevenness of the bond between the piezoelectric element and transducer cap is similarly visible from the temperature profile variations for different diameter lines.

3.2. Thermal camera measurements

Images of the transducer cap were taken using a thermal camera for modes at 320 ± 10 kHz and 6.77 ± 0.01 MHz for comparison with the results from the TLC sensor. Images were first taken with just black paint on the cap to ensure constant infrared emissivity and measure the overall temperature change on operation of the transducer, and then with the backing layer of the compound TLC sensor to measure heat

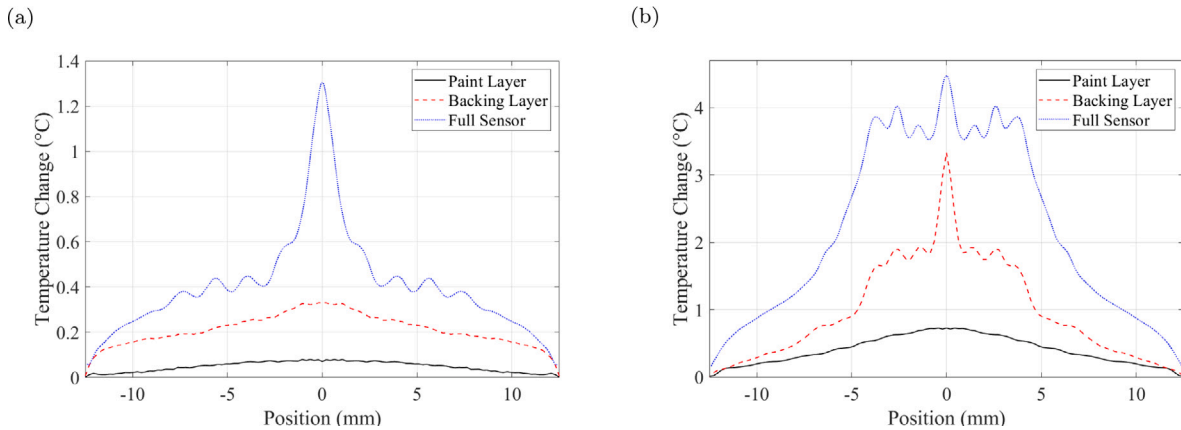


Fig. 11. Average temperature change across multiple diameters for (a) the 320 ± 10 kHz mode and (b) the 6.77 ± 0.01 MHz mode. Solid black line shows thermal camera data for the transducer cap with just a layer of black paint, dashed red line shows thermal camera data for the cap with the backing layer. The dotted blue line shows data from the TLC sensor.

absorption in this layer. The images were analysed in a similar way to the temperature change across the diameter shown in Figs. 9(c) and 10(c), with the average temperature change measured across multiple diameters plotted in Fig. 11(a).

For the mode at 320 ± 10 kHz, the solid black line in Fig. 11(a) shows the average temperature change for different diameters taken across the transducer cap with a black paint layer. The temperature across the centre of the cap (central 5 mm diameter) is even, with a linear diffusion of heat from the edge of this area to the outer edge of the transducer cap. This is expected since the majority of the mechanical heating is generated by the piezoelectric element, which has a 9 mm diameter and is bonded to the centre of the cap. The red dashed line in Fig. 11(a) shows the average temperature change for the transducer cap with the backing layer on top. The total temperature change for the backing layer is around four times that measured with just the paint layer, demonstrating absorption of ultrasound in the backing layer. The linear heat diffusion towards the edges of the cap is still visible, but some features of the mode (peaks in the temperature change) are visible, most notably in the centre of the transducer where the ultrasound amplitude is largest. Finally, the dotted blue line shows the calculated average temperature change across the transducer diameter for the full TLC sensor. The details of the mode are clear, with the peaks representing the anti-nodal rings. The temperature change for the TLC sensor at the centre is about four times the temperature change of the backing layer alone, and sixteen times that of the cap with just the paint layer. This shows that, whilst the backing layer improves the efficiency of the sensor, particularly at lower frequencies [28], absorption also occurs within the LC layer.

Temperature analysis for the mode at 6.77 ± 0.01 MHz is shown in Fig. 11(b). The linear diffusion of heat from the centre of the cap to the edge is more pronounced, along with there now being a linear diffusion of heat across the piezoelectric element itself. This is expected since, as shown by Eq. (3), at higher frequencies less power is required for larger absorption of the ultrasound in the sensor, therefore more heating would be observed. The average temperature change for the cap with the backing layer on top is displayed by the red dashed line in Fig. 11(b). For this frequency the mode peaks are visible for analysis of the backing layer without LC, indicating that more ultrasound is absorbed in the backing layer at this higher frequency. This is also expected from Eq. (3), as at higher frequencies less power is required to obtain similar amplitudes. There may also be larger heat losses in the piezoelectric element when driven so far from its 40 kHz fundamental frequency. The analysis of the full TLC sensor is shown by the blue dotted line in Fig. 11(b). The mode peaks are also observed when using

the full TLC sensor. Similarly to the 320 ± 10 kHz mode, absorption is increased with the use of the full sensor.

3.3. Comparison of ultrasonic displacement and temperature change

Displacement measurements were taken using interferometry for modes at 320 ± 10 kHz, 420 ± 10 kHz, and 6.77 ± 0.01 MHz, in order to perform an initial comparison of the ultrasonic displacement and the temperature change. The loading of the sensor on to the transducer cap causes a shift in the frequency of the cap resonance [42], due to a combination of additional mass (which would shift the frequency upwards) and damping (which can shift the frequency down). Hence several measurements were taken on either side of the target frequency. The frequencies of the resonant modes found using interferometry measurements were higher than those found using the TLC sensor, implying that the damping introduced by the sensor had the greatest effect on the frequency shift.

Fig. 4(c) shows the two perpendicular diameter lines along which displacement data was obtained, with the average taken to account for some of the variability in coupling between the piezoelectric transducer and the aluminium cap. Fig. 12 shows the displacement (black line, left hand axis) and the average temperature change from the TLC analysis (red line, right hand axis). The interferometry displacement measurements have a resolution of 0.02–0.04 nm, with higher resolution at higher frequencies due to reduced step size between measurements. The thermal background not related to ultrasound absorption was removed from the temperature change lines for the TLC data. This was done by fitting a low order polynomial to the data shown in Figs. 11(a) and 11(b) to remove background heating due to thermal conductivity, whilst maintaining the features of the mode resulting from ultrasound absorption in the sensor for easier comparison with the displacement data.

For the lower frequencies, 320 ± 10 kHz (Fig. 12(a)) and 420 ± 10 kHz (Fig. 12(b)), the positions of the peaks in the interferometer and TLC data correlate. However, the temperature data from the TLC sensor has a large amplitude central peak and smaller peaks away from the centre when compared to the displacement measurement. This is likely due to a combination of the damping caused by placing the sensor on the cap, and the high thermal conductivity of the transducer (247 W/K/m) reducing the thermal contrast and therefore the observed amplitude. To compare resolution, the average full width half maximum (FWHM) values were calculated using several peaks (omitting the central peak). For 320 ± 10 kHz this gave a FWHM of 0.94 ± 0.06 mm for the displacement data, and 0.88 ± 0.03 mm for the temperature change,

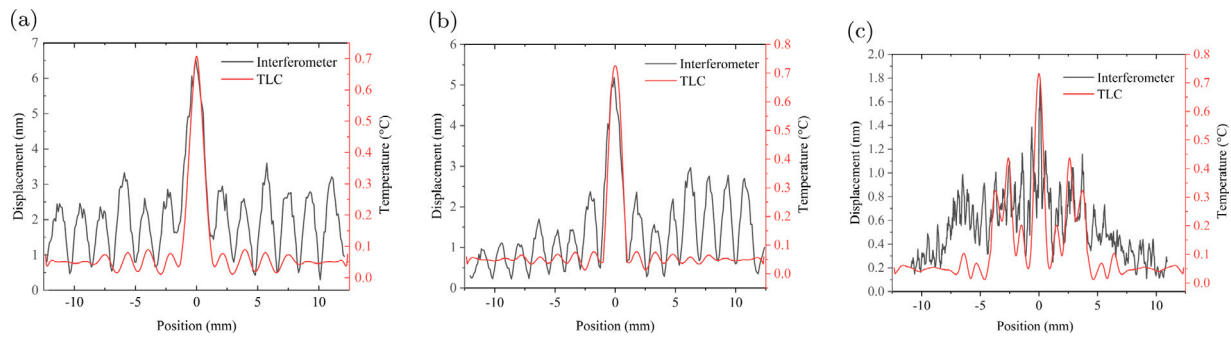


Fig. 12. Comparison of average displacement across multiple diameters using interferometry (black line, left axis) and average temperature change for the TLC sensor (red line, right axis) for modes at frequencies (a) 320 ± 10 kHz, (b) 420 ± 10 kHz, and (c) 6.77 ± 0.01 MHz.

while for 420 ± 10 kHz the FWHM were 0.8 ± 0.1 mm and 0.80 ± 0.03 mm respectively. This confirms that the TLC sensor is able to resolve sub-millimetre sized features, with the images being a good representation of the mode shape.

For the higher frequency mode at 6.77 ± 0.01 MHz, shown in Fig. 12(c), the interferometry data shows a more detailed mode pattern with many narrow mode features, as would be expected for higher frequency modes. The peak structure is unlikely to be noise due to the fact similar features are observed either side of the central point. The TLC data demonstrates the limit on resolution, showing peaks relating to the envelope of the interferometry scan. Since the droplets in the sensor are $3\text{--}5$ μm in diameter, the resolution is not limited by the sensor itself. Therefore, the reduction of resolution here is likely the result of the thermal conductivity of both the cap and the sensor, which can be seen in more detail in Fig. 11(b). Heat diffuses laterally across the cap, and obscures the finer details that are visible from the interferometry scan.

4. Conclusion

A compound TLC sensor was built, and a method to convert optical images of the sensor was developed. The sensor was used to measure the displacement of several resonant modes of a flexural ultrasonic transducer, for a frequency range from 320 ± 10 kHz to 6.77 ± 0.01 MHz. The local temperature change of the sensor is due to absorption of ultrasound within the backing layer and the LC layer, and depends primarily on ultrasonic displacement, along with other factors such as the coupling and frequency of operation. Thermal imaging measurements showed absorption of ultrasound when using just the backing layer, with additional absorption shown when using the full sensor. The thermal conductivity of the cap displayed linear heat diffusion from the centre of the cap to the edge, which increases at higher frequencies. Comparative displacement information was extracted from images of the TLC sensor on the transducer cap as a temperature map, and compared with the displacement measured using interferometry. Excellent agreement of resonant mode pattern position was observed at the lower frequencies, 320 ± 10 kHz and 420 ± 10 kHz. The TLC sensor data at a higher frequency of 6.77 ± 0.01 MHz showed an envelope of the interferometry data, due to lateral heat diffusion in the transducer cap and sensor. The minimum observed resolution of the sensor was 0.80 ± 0.03 mm.

The sensors show promise for quick and low cost visualisation of 2D ultrasonic fields, such as for transducer characterisation. The field generated from a transducer is typically mapped using a hydrophone [5], with this paper showing a faster possible alternative. At higher frequencies an envelope of the displacement data was observed, however, this would still provide useful information about the focus of the beam for safety determination. Where full quantification is required, other methods such as scanning laser doppler vibrometry (SLDV) could be used, following initial screening using the TLC sensors.

Other applications for the sensor include structural health monitoring by using the sensor in the form of a smart paint, giving a visual image of regions where ultrasound is blocked by an internal defect, or where surface wave amplitude is enhanced due to constructive interference between incident and reflected waves [43]. The theoretical resolution of the sensor should be significantly higher than that of data taken with a microphone or hydrophone, since resolution is dependent on liquid crystal droplet size [22], with the main limitations resulting from the thermal conductivity of the sample the sensor is placed upon. Since the sensor is passive, it is ideal for in-situ measurements, requiring only an optical camera and suitable lighting for data capture, with the method of generation able to be adjusted to suit the environment. The visual nature will also allow for future automation through the use of robotic vision.

CRedit authorship contribution statement

M. Turvey: Writing – original draft, Software, Methodology, Investigation, Formal analysis, Data curation. **O. Trushkevych:** Writing – review & editing, Supervision, Methodology, Conceptualization. **D.J. McKnight:** Methodology. **R.S. Edwards:** Writing – review & editing, Supervision, Project administration, Methodology, Funding acquisition, Conceptualization.

Declaration of competing interest

The authors declare that they have no known competing financial interests or personal relationships that could have appeared to influence the work reported in this paper.

Data availability

Data will be made available on request.

Acknowledgments

This work was funded via the Future Innovation in NDE Centre for Doctoral Training (FIND-CDT), (EPSRC EP/S023275/1). MT thanks FIND-CDT for funding her PhD.

References

- [1] J.E. Michaels, Ultrasonic wavefield imaging: Research tool or emerging NDE method? in: AIP Conference Proceedings, AIP Publishing LLC, 2017, 020001.
- [2] B.G. Tomov, S.E. Diederichsen, E. Thomsen, J.A. Jensen, Characterization of medical ultrasound transducers, in: 2018 IEEE International Ultrasonics Symposium, IUS, IEEE, 2018, pp. 1–4.
- [3] P. Murali, J. Baborowski, Micromachined ultrasonic transducers and acoustic sensors based on piezoelectric thin films, J. Electroceram. 12 (1) (2004) 101–108.
- [4] J.K. Na, J.L. Blackshire, S. Kuhr, Design, fabrication, and characterization of single-element interdigital transducers for NDT applications, Sensors Actuators A 148 (2) (2008) 359–365.

- [5] A. Shaw, M. Hodnett, Calibration and measurement issues for therapeutic ultrasound, *Ultrasonics* 48 (4) (2008) 234–252.
- [6] H. Mei, M.F. Haider, R. Joseph, A. Migot, V. Giurgiutiu, Recent advances in piezoelectric wafer active sensors for structural health monitoring applications, *Sensors* 19 (2) (2019) 383.
- [7] T. Di Ianni, L. De Marchi, A. Perelli, A. Marzani, Compressive sensing of full wave field data for structural health monitoring applications, *IEEE Trans. Ultrason. Ferroelectr. Freq. Control* 62 (7) (2015) 1373–1383, <http://dx.doi.org/10.1109/TUFFC.2014.006925>.
- [8] H. Xu, L. Liu, X. Li, Y. Xiang, F.-Z. Xuan, Wavefield imaging of nonlinear ultrasonic Lamb waves for visualizing fatigue micro-cracks, *Ultrasonics* 138 (2024) 107214.
- [9] W.J. Staszewski, R. bin Jenal, A. Klepka, M. Szewdo, T. Uhl, A review of laser Doppler vibrometry for structural health monitoring applications, *Key Eng. Mater.* 518 (2012) 1–15.
- [10] Y.-K. Zhu, G.-Y. Tian, R.-S. Lu, H. Zhang, A review of optical NDT technologies, *Sensors* 11 (8) (2011) 7773–7798.
- [11] G. Wissmeyer, M.A. Pleitez, A. Rosenthal, V. Ntziachristos, Looking at sound: optoacoustics with all-optical ultrasound detection, *Light: Sci. Appl.* 7 (1) (2018) 1–16.
- [12] R. Lal, D. Das-Gupta, Characterization of ultrasonic transducers, *IEEE Trans. Electr. Insul.* 24 (3) (1989) 473–480.
- [13] A.R. Selfridge, Wave field visualization using scanned hydrophone measurements, in: *Medical Imaging 1999: Ultrasonic Transducer Engineering*, SPIE, 1999, pp. 202–209.
- [14] R. Wyatt, Visualization of pulsed ultrasound using stroboscopic photoelasticity, *Non-Destr. Test.* 5 (6) (1972) 354–358.
- [15] Y.-H. Nam, S. Lee, A quantitative evaluation of elastic wave in solid by stroboscopic photoelasticity, *J. Sound Vib.* 259 (5) (2003) 1199–1207.
- [16] J.S. Sandhu, H. Wang, W.J. Popek, P.J. Sincebaugh, Acoustography: a side-by-side comparison with conventional ultrasonic scanning, in: *Nondestructive Evaluation of Aging Materials and Composites Iii*, SPIE, 1999, pp. 163–172.
- [17] J. Sandhu, H. Wang, Recent advances in acoustography-based NDE, in: *Recent Advances in Experimental Mechanics: In Honor of Isaac M. Daniel*, Springer, 2002, pp. 381–388.
- [18] J.S. Sandhu, R.W. Schoonover, J.I. Weber, J. Tawiah, V. Kunin, M.A. Anastasio, Transducer field imaging using acoustography, *Adv. Acoust. Vib.* 2012 (2012).
- [19] A. Poudel, S.S. Shrestha, J.S. Sandhu, T.P. Chu, C.G. Pergantis, Comparison and analysis of acoustography with other NDE techniques for foreign object inclusion detection in graphite epoxy composites, *Composites B* 78 (2015) 86–94.
- [20] Y.J. Liu, X. Ding, S.-C.S. Lin, J. Shi, I.-K. Chiang, T.J. Huang, Surface acoustic wave driven light shutters using polymer-dispersed liquid crystals, *Adv. Mater.* 23 (14) (2011) 1656–1659.
- [21] O. Trushkevych, T. Eriksson, S. Ramadas, S. Dixon, R. Edwards, Ultrasound sensing using the acousto-optic effect in polymer dispersed liquid crystals, *Appl. Phys. Lett.* 107 (5) (2015) 054102.
- [22] R. Edwards, J. Ward, L. Zhou, O. Trushkevych, The interaction of polymer dispersed liquid crystal sensors with ultrasound, *Appl. Phys. Lett.* 116 (4) (2020) 044104.
- [23] B. Cook, R. Werchan, Mapping ultrasonic fields with cholesteric liquid crystals, *Ultrasonics* 9 (2) (1971) 88–94.
- [24] Y. Kagawa, T. Hatakeyama, Y. Tanaka, Detection and visualization of ultrasonic fields and vibrations by means of liquid crystals, *J. Sound Vib.* 36 (3) (1974) 407–416.
- [25] R. Denis, Characterization of ultrasonic transducers using cholesteric liquid crystals, *Ultrasonics* 16 (1) (1978) 37–43.
- [26] M.E. Haran, Visualization and measurement of ultrasonic wavefronts, *Proc. IEEE* 67 (4) (1979) 454–466.
- [27] J. Kim, M. Kim, Focal position control of ultrasonic transducer made of plano-concave form piezoelectric vibrator, *Ultrasonics* 121 (2022) 106668.
- [28] O. Trushkevych, M. Turvey, D.R. Billson, R. Watson, D.A. Hutchins, R.S. Edwards, Acoustic field visualisation using local absorption of ultrasound and thermochromic liquid crystals, *Ultrasonics* (2024) 107300.
- [29] P.J. Collings, J.W. Goodby, *Introduction to Liquid Crystals: Chemistry and Physics*, Crc Press, 2019.
- [30] I. Sage, Thermochromic liquid crystals, *Liq. Cryst.* 38 (11–12) (2011) 1551–1561.
- [31] M. Eames, Z. Larrabee, A. Hananel, F. Padilla, J.-F. Aubry, Low-cost thermochromic quality assurance phantom for therapeutic ultrasound devices: A proof of concept, *Ultrasound Med. Biol.* 49 (1) (2023) 269–277.
- [32] Assortment set, liquid crystal sheet, 2023, <https://www.edmundoptics.co.uk/p/assortment-set-liquid-crystal-sheet/16688/>. (Accessed: 17 January 2023).
- [33] A. Feeney, L. Kang, S. Dixon, Higher order modal dynamics of the flexural ultrasonic transducer, *J. Phys. D: Appl. Phys.* 55 (7) (2021) 07LT01.
- [34] A.W. Leissa, *Vibration of plates*, Scientific and Technical Information Division, National Aeronautics and Space Administration, Washington, 1969.
- [35] A.P. Cracknell, *Ultrasonics*, Wykeham Publication (London) Ltd., 1980.
- [36] T.R. Neil, Z. Shen, D. Robert, B.W. Drinkwater, M.W. Holderied, Moth wings as sound absorber metasurface, *Proc. R. Soc. Lond. Ser. A Math. Phys. Eng. Sci.* 478 (2262) (2022) 20220046.
- [37] G. Wyszecki, W.S. Stiles, *Color Science: Concepts and Methods, Quantitative Data and Formulae*, second ed., Wiley, New York, 1982.
- [38] J. Feather, M. Hajizadeh-Saffar, G. Leslie, J. Dawson, A portable scanning reflectance spectrophotometer using visible wavelengths for the rapid measurement of skin pigments, *Phys. Med. Biol.* 34 (7) (1989) 807.
- [39] M. Tkalcic, J. Tasic, Colour spaces: perceptual, historical and applicational background, in: *The IEEE Region 8 EUROCON 2003. Computer as a Tool*, 2003, pp. 304–308, <http://dx.doi.org/10.1109/EURCON.2003.1248032>.
- [40] A.K.R. Choudhury, *Principles of Colour and Appearance Measurement: Object Appearance, Colour Perception and Instrumental Measurement*, Elsevier, 2014.
- [41] J. Schanda, *Colorimetry: Understanding the CIE System*, John Wiley & Sons, 2007.
- [42] A. Karle, S. Bhoite, A. Amale, An analysis of transducer mass loading effect in shaker testing, *J. Eng. Res. Appl.* 4 (6) (2014) 207–212.
- [43] R. Edwards, X. Jian, Y. Fan, S. Dixon, Signal enhancement of the in-plane and out-of-plane Rayleigh wave components, *Appl. Phys. Lett.* 87 (19) (2005) 194104.